Contract No.:

This manuscript has been authored by Battelle Savannah River Alliance (BSRA), LLC under Contract No. 89303321CEM000080 with the U.S. Department of Energy (DOE) Office of Environmental Management (EM).

Raman Signatures of Detonation Soot

Eliel Villa-Aleman*[a], Jason R. Darvin[a], Michael H. Nielsen[b], and Trevor M. Willey[b]

[a]Savannah River National Laboratory
Aiken, SC 29808 United States

[b]Lawrence Livermore National Laboratory
Livermore, CA 94550 United States

*Corresponding Author: Eliel Villa-Aleman

Abstract

Soot generated from the detonation of nine explosives was investigated with Raman micro spectroscopy and high-resolution transmission electron microscopy (HRTEM). The first order bands, located at approximately 1580 (G), 1350 (D1), 1620 cm^{-1} (D2), 1500 (D3), and 1200 (D4), are used to provide information on the carbon allotropes and defects. The intensity ratios and the full-width at half-maximum provide an indication of the disorder in the material. The Raman spectra of soot acquired from the detonation of nine explosives showed differences which can be used to identify the precursor explosive. Most differences in the spectra were correlated with the presence of amorphous carbon in the soot. In additional to identification of distinct bands in the spectra via deconvolution, principal component analysis was also used to differentiate the different types of soot. HRTEM performed on soot samples with different explosive precursors identified several distinct allotropes of carbon such as nanodiamonds, carbon onions, graphite fibers, and amorphous carbon.

Keywords: explosives, soot, Raman spectroscopy, principal component analysis

Introduction

The identification of explosives post detonation is of interest to law enforcement agencies and many government entities. Identification of the explosive used can provide investigators with information related to the perpetrators and their motivation. Ideally, explosive residue will be left behind giving investigators a small sample of the explosive material to work with; however, it is possible that only detonation soot is left behind. Soot is defined as the carbonaceous material that remains after the incomplete combustion of a carbon containing material. Many studies have shown that soot generated from a wide variety of materials contain similar properties, and Raman spectroscopy is commonly employed to investigate carbon allotropes and the properties of soot after combustion.[1-16] Raman spectroscopy can yield molecular structure information based on the full-width half-maximum (FWHM) and the intensity of the four defect and graphite bands. Several literature sources propose the graphite (G)[12,17] and defect bands (D1[12,17], D2[17], D3[18,19], D4[2,7,19]) are located at approximately 1580, 1350, 1620, 1500, and at 1200 cm^{-1}, respectively. In a typical Raman spectrum of soot, the five bands are convoluted where the D1 and G bands are the most intense in the spectrum. The defect bands are related to specific molecular changes in the structure of graphite. The Raman bands corresponding to the D bands become, D1, disordered edge layers of a graphene sheet, D2, disordered surface layer of a graphene sheet, D3, amorphous carbon, and D4, sp_2 – sp_3 bonds of a disordered graphitic lattice originating from polyene-like structures. Attempts have been made to correlate the band position, FWHM, and intensity of the bands with the material properties. The D1/G band intensity ratio has been used to attempt to identify the degree of structurization of carbon in soot samples as well as the FWHM of the D1 band. These attempts to correlate spectral parameters with the structure of the primary carbon allotropes have been found to be unreliable for distinguishing soots with visually similar spectra.[5]

An additional problem often observed in the characterization of soot via band characterization is the reproducibility of the spectra and statistical uncertainties associated with nonlinear fitting procedures.[5] Multivariate statistical methods are widely used for classification purposes with spectroscopic data. Principal component analysis (PCA) is a statistical method commonly used to classify Raman spectral data[20-22] and has been described in great detail previously.[23,24] Briefly, PCA is a non-parametric statistical method that performs dimensionality reduction on a large data set. First, the covariance matrix is computed; the eigenvectors and eigenvalues of the covariance matrix are then computed to determine the principal components of the data. These principal components represent features of the spectral data. Small variations in the data are captured allowing for classification of spectral data sets that all share common characteristics.

Materials and Methods

The explosives used for this study are: ultrafine TATB (UFTATB), 95% TATB 5% Kel F-800 (TATB), 95% HMX 4.5% estane 0.5% polyurethane (HMX), DNTF, HNS IV, 60% TNT 40% RDX (Comp B), 94% LLM-105 6% viton-A (LLM-105), FOX-7, and TNT. Table 1 shows the explosives used in this research and their primary carbonaceous species in the detonation soot. The explosives were placed into an open bore within an ice block, and the ice block was placed into an aluminum vessel prior to detonation to minimize the environmental carbon collected

during recovery of the soot. Ice blocks were cut in half to recover the detonation soot. The recovered soot was preserved as a suspension in water for further analysis. Previously published work provides additional details of the detonation and soot collection.[25]

Raman Spectroscopy:

Aliquots of soot suspended in water were deposited onto a polished metal surface and allowed to dry before Raman measurements were made. The Raman measurements were made at several different spots on each soot sample. Micro-Raman spectra were obtained with a LabRAM HR800 UV (Horiba Scientific). An iDus detector (DU416A-LDC-DD from Andor) with a 1600x400 pixel array was used for collection of the data. The detector's pixels have 15 μm resolution. The Andor detector was cooled to -95 °C. Labspec 5.78 (HORIBA Scientific) software was used to control the spectrometer and detector. The laser was focused on the sample with an Olympus LMPLFLN 50x objective with NA = 0.5. The laser power density was ≤ 0.064 $W/\mu m^2$. A grating with 1800 g/mm and blazed to 500 nm was used in the spectrometer. The spectral profile of the laser beam was cleaned up with a bandpass filter. An ultrasteep long-pass edge filter (Semrock) was used to measure the Raman signal down to 100 cm^{-1}. The laser power measured at the sample was between 0.5 and 1 mW and focused with a 50x microscope objective. Spectral calibration was conducted with the 520.7 cm^{-1} band of silicon. The spectra were not calibrated for intensity.

The auto-overlap and combination of 3 spectra were taken using the "auto" mode of the scan. The range of the acquired spectra was 250 – 3750 cm^{-1} and the acquisition time per spectrum was 1 hour. Spectra were collected at low (0.5 mW), medium (1 mW), and high (2 mW) laser powers to ensure long acquisition times did not lead to sample heating and spectral artifacts. Spectral artifacts did occur at high laser powers. Ten spots on the sample were randomly selected for analysis at low to medium laser power to ensure heating did not introduce artifacts to the data. A typical acquisition of the 10 spots was thus conducted in ~10 hours. Samples were analyzed with 405 nm and 514 nm diode lasers. Soot from different explosives showed different types of fluorescence, and the spectra of the fluorescence observed in the samples varied in intensity and spectral content.

High-Resolution Transmission Electron Microscopy:

Electron microscopy was conducted on a JEOL 2100-F field emission TEM operating at 200 kV and equipped with an Orius SC1000 CCD and GIF Tridiem spectrometer (Gatan Inc.).

Data Analysis Methods

Baseline correction was conducted to remove the fluorescence in the spectra using OriginPro. Following baseline collection, a Savitzky-Golay filter was used to smooth the spectra. Smoothed spectra were normalized to 1 at ~1600 cm^{-1} (G band). Representative spectra for each wavelength after correction are shown in Figure 1. Fluorescence can be significant in the spectra as shown in SI Figure 1a and 2a. The spectra were baseline corrected, smoothed, normalized, and chopped from the range of 1000 – 2000 cm^{-1} for the 405 nm data and 800 – 2000 cm^{-1} for the 514 nm data for further analysis. Representative spectra are shown for each step of preprocessing in SI Figure 1 for the 405 nm data and SI Figure 2 for the 514 nm data. Visual outliers, indicated by the presence of additional erroneous peaks or no signal, were eliminated from the analysis. Principal component

analysis was performed using PLS_Toolbox in MATLAB. A total of 72 spectra were used for the 514 nm data and 72 spectra for the 405 nm data during the analysis. The methodology for the analysis of the spectra acquired with the 514 nm laser was modified slightly for the analysis of the data acquired with the 405 nm laser. The 1st derivative of the 405 nm data was taken before PCA analysis. This minor modification was made to improve the peak separation in the PCA space. Spectral deconvolution was performed using GRAMS/AI™ spectroscopy software.

Results and Discussion

Sadezky *et. al.* have shown that the Raman spectra of soot is primarily made up of five bands known as the G, D1, D2, D3, and D4 bands.[5] The G band (~1580 cm^{-1}) originates from the ideal graphitic lattice. The D1 band (~1350 cm^{-1}), the D2 band (~1620 cm^{-1}), and the D4 band (~1200 cm^{-1}) originated from disordered graphitic lattices. Finally, the D3 band (~1500 cm^{-1}) originates from amorphous carbon. It should be noted the aim of this work was not to fit the bands for each soot. According to Sadezky et al., a visual examination of the data shows that soots containing amorphous carbon have a higher intensity around 1500 cm^{-1} as shown in Figure 2. Sadezky *et. al.* also observed three additional bands when Raman spectra were recorded with a 514 nm laser at about 2450, 2720, and 3250 cm^{-1}. The band located around 2450 cm^{-1} was attributed to the first overtone of the Raman inactive lattice vibration mode located around 1220 cm^{-1}. The band located near 2720 cm^{-1} was attributed to the first overtone of the D1 band, and the band located near 3240 cm^{-1} to the first overtone of the D2 band. The overtone bands were observed as seen in Figure 1. Their location and appearance is consistent with literature reports.[5] SI Figure 1a and SI Figure 2a show some soots spectra were dominated by fluorescence in the region where the overtone bands appear. The high level of fluorescence in those soots results in a lower signal to noise ratio which would lead to greater variability in any analysis of those bands. For those reasons, the overtone bands were not analyzed in this work.

Typically, the initial spectral analysis of this work aimed to identify any variances in the data from different spatial regions of the soot deposited on the smooth steel plate. Raman spectra from ten spots were acquired to identify band intensity variation but also to identify potential band ratios from the different spectra. The spots analyzed on the sample with a 50x objective were approximately 5 μm in diameter, significantly larger than the typical graphite crystallite dimensions of ~10 nm. Additional spatial regions of the soot were selected to ensure the acquired Raman spectra did not significantly vary. Since autofocusing was not available with the microscope, the intensity of the spectra changed due to focusing conditions although the relative intensity of the bands remained approximately the same. Figure 1 shows representative spectra for each soot analyzed from the different explosives. The fluorescent intensity for different spots within the same soot varied.

Several soot samples demonstrated significant fluorescence intensity with the 514 nm excitation laser. The order of the fluorescence intensity for the soot samples was established as UFTATB, HMX, LLM-105, Comp B, DNTF, TATB, TNT, HNS IV, and FOX-7. Fluorescence was not observed from HNS IV, FOX-7, and TNT at this wavelength. The common denominator for the non-fluorescent soot with the 514 nm excitation laser is the graphite content where HNS IV is characterized with graphite fibers, and FOX-7 and TNT with graphite. Interestingly, Comp B

which is a 60:40 TNT/RDX mix shows fluorescence suggesting that RDX or reaction products between Comp B and RDX are responsible for fluorescence in the Comp B analysis. Fluorescence observed from soot can be the result of the presence of polycyclic compounds in the sample,[1,4,26] or it can result from hydrogenated forms of carbon.[27,28] In this set of experiments, the observed lack or presence of fluorescence provides further signatures in the identification of the precursor explosive. The spectra of the soot acquired with the 405 nm showed different fluorescence behavior. The order of fluorescent intensity was established as HMX, DNTF, UFTATB, Comp B, FOX-7, LLM-105, TATB, HNS IV, and TNT. UFTATB and Comp B exhibited the same amount of fluorescence while fluorescence was not observed for HNS IV and TNT at 405 nm excitation. FOX-7 displayed a very small amount of fluorescence with 405 nm excitation.

Figure 2 shows the spectra of soot in the 800 – 2000 cm^{-1} spectral range for data collected with the 514 nm excitation laser and 1000 – 2000 cm^{-1} for data collected with 405 nm excitation laser. The data shows the intensity of the defect bands relative to the G band at 1580 cm^{-1}. The main spectral differences among the different types of soot are the valley region at ~1500 cm^{-1}, the intensity of the D1 band, and the shift of the intensity in the 1200 cm^{-1} region corresponding to the D4 band region. Soot spectra acquired with the 405 nm excitation laser exhibited similar behavior to the soot acquired with the 514 nm laser, although the D1 band intensity was smaller and shifted closer to the G band. The observations are in agreement with the wavelength dependence of the D1 band intensity and location described in the literature.[5]

The behavior of the intensities, locations, and the FWHMs of the bands in the spectra from the different types of soot is consistent with formation of different carbon allotropes at the molecular level. [1,10-12,17,19,29-35] The relative abundance of the amorphous carbon content in the sample correlates with the intensity of the valley region around 1500 cm^{-1} and the results are shown in Figure 3 for the soots with the lowest (Comp B) and highest (TATB) amounts of amorphous carbon. Following the method of Sadezky *et. al.*, bands D1, D2, D4, and G were fit using a Lorentzian function and the D3 band was fit using a Gaussian function.[5] All spectra collected for a given soot were averaged prior to spectral fitting. Also, the FWHM of the D1 and the G band regions are affected by the amorphous formation, and similarly the D4 region located at approximately 1200 cm^{-1}. The small spectral deviations observed from the ten spectra acquired for each detonation soot suggests that the explosive in the device experienced uniform thermodynamic conditions during the detonation. Otherwise, the spectral separation among the different types of soot would have been meaningless due to the high intra-sample variability. Although the data analyzed comes from soot originating from the detonation of small devices, the results are likely applicable to the detonation of larger devices as well. Oxidation of the soot from a prolonged high temperature detonation might change the thermodynamics and affect the spectral characterization of the soot. The data from these experiments clearly show that Comp B and HNS IV have the minimum amount of amorphous carbon based on the intensity of the 1500 cm^{-1} valley. In order to ensure that the results are consistent using different excitation wavelengths, the valley intensity was compared for the spectra acquired with the 514 and 405 nm excitation lasers. Figure 4 shows the relative valley intensities for each excitation laser wavelength for the different types of soot. The trends for the 405 and 514 nm wavelengths are

generally parallel, suggesting that analysis of data at different wavelengths produces similar results. The spectral characterization of the soot and correlation with prevalence of amorphous carbon is consistent with the TEM analysis of these samples. It should be noted that while nanodiamond was found to be the primary carbon form found in comp B, a sharp diamond peak was not observed because the Raman cross section of sp^2 carbon is up 200 times greater than that of sp^3 carbon at visible wavelengths.[36] The other primary nanostructures observed are additionally shown in Figure 5, carbon onions from the DNTF soot and amorphous carbon from the detonation of UFTATB.

Representative transmission electron microscopy images of different categories of nanocarbon particulates found in the soot samples are shown in Figure 5. Consistent with previous reports,[25,37-40] TEM observations revealed a mixture of different carbon allotropes present in the soots of most explosives. Mixtures of nanodiamond and graphite fibers were observed in soots generated by Comp B, HNS IV, TNT, and FOX-7.[12,36-43] Soots of TATB, UFTATB, and LLM-105 likewise contained these allotropes in addition to substantial amounts of amorphous carbon.[37,44,45] HMX produced a soot that was a menagerie of all three as well as large, stacked graphite sheets. The major exception to the broad heterogeneity of the soots was DNTF which produced a soot that was almost completely composed of graphitic, onion-like carbon, with a very minute fraction of diamond observed.[39,40,46,47]

Despite the presence of different types of carbon, most soots had a predominant type of carbon that was observed through extensive imaging, diffraction, and electron energy loss spectroscopy. As has been well-documented elsewhere, Comp B soot was found to have a large fraction of nanodiamond.[36,42] By contrast, HNS IV, TNT, and FOX-7 were observed to have a substantial population of graphite fibers. HMX had a broad mixture of different particulates and it would be difficult to determine a predominate allotrope or morphology based on TEM measurements. TATB, UFTATB, and LLM-105 soots contained a substantial amount of structures that were amorphous in character. Finally, while nanodiamonds were very occasionally observed in DNTF soot, onion-like carbon was the overwhelmingly predominant particulate throughout the sample.

Principal Component Analysis (PCA) is a tool that helps visualize and extract information from a given explosives (e.g., soot) data set. PCA is a dimensionality reduction method that retains features and patterns within a data set; it accomplishes data reduction by projecting the data onto lower dimension data planes. Each of these new planes are referred to as principal components (PC). Principal components are a linear combination of the original data and are calculated by determining the direction in which the variance of a data plane is the greatest. Each principal component is orthogonal to the preceding principal component. The resulting principal components can then be plotted to identify trends in data that were indistinguishable with the original data. The applicability of PCA to the data from different types of soot from detonation shots can provide an image where different measurements can be extracted in a subspace. PCA was used to differentiate the different types of soot generated from each explosive by identifying correlations between subsets of the data. PC 1 was found to capture 96.99 % of the variance for the 405 nm data and 99.70% of the variance for the 514 nm data. This result is expected given each spectrum shares the same major characteristics and mean centering was not performed on

the data; thus, PC1 is characterized by the overall shape of the spectra. Similarly, Grafen *et. al.* used PCA to analyze the Raman spectra of soot derived from diesel engines and found that PC1 captured ~99.5% of the variance.[3] Figure 6 displays the scores plot of PC3 vs. PC2 for the 405 and 514 nm data. PC2 captured 1.36 % for the 405 nm data and 0.17 % of the variance for the 514 nm data. PC 3 captured 0.86 % for the 405 nm data and 0.05 % for the 514 nm. By plotting the PC2 and PC3 values for a given measurement together, the soot originating from different precursor explosives can be distinguished based on the aggregation of points in the PCA diagram.

Principle Component Analysis score plots for the data acquired at 405 nm and 514 nm laser excitation energy are shown in Figure 6a and 6b, respectively. Inclusion of the overtone bands did not allow for differentiation. Scores plots using PC1 did not allow for differentiation but are shown in SI Figure 3 for 405 nm data and SI Figure 4 for 514 nm data. Loading plots for PC1, PC2, and PC3 are shown in SI Figure 5 for the 405 nm data. The first derivative of the 405 nm data was used for PCA, so a straightforward comparison to the original data cannot be made. First derivative values of zero indicate a local maximum or local minimum of the original spectra. The loading values of PC1 for the 405 nm data, are identical to the derivative of the data, albeit mirrored, indicating small variations in the overall shape of the data are responsible for the scores of PC1. The loading values of PC2 for the 405 nm data intersect zero at 1317, 1379, 1470, 1530, 1581, and 1628 cm^{-1}. The loadings values of PC3 for the 405 nm data intersect zero at 1550 and 1623 cm^{-1}. Analyzing the loading plots for the 514 nm data is easier because the data used for PCA was not preprocessed by taking a derivative. The loading plots for the 514 nm data are shown in SI Figure 6. As with the 405 nm, the loading values for PC1 for the 514 nm resemble the average of all spectra indicating scores for PC1 are a result of minor changes in the overall shape of each spectrum. The loadings values for PC2 assign positive values at 1346 and 1600 cm^{-1} and negative values at 1232, 1492, and 1660 cm^{-1}. The positive values at 1346 cm^{-1} could be caused by the contribution of the D1 band and the positive values at the 1600 cm^{-1} are likely to be caused by contributions of the G band. Negative values for PC2 at 1232 cm^{-1} are caused by the contribution of the D4 band, negative values at 1492 cm^{-1} are a result of contributions of the D3 band, and negative values at 1660 cm^{-1} are cause by contributions of the D2 band. The loading values for PC3 at 514 nm assign positive values at 1247 and 1628 nm. Negative values are assigned at 1349 and 1561 cm^{-1}. The values indicate that the broadest soot spectrum result in higher PC3 values. The loading values for PC3 show nearly zero contribution at 1428 cm^{-1} indicating that the D3 band (amorphous carbon) does not contribute to the values of PC3.

The location of the points in the diagram and the data scatter each provide information on the given explosives. For instance, HMX has a large scatter of the data points for both the 405 nm and 514 nm excitation. HRTEM indicates the existence of diamonds, graphite fibers, amorphous/weakly graphitic carbon, and large, stacked graphite sheets. Therefore, it is possible that different measurements were influenced by the different types of carbon allotropes. Detonation soot from UFTATB, HMX, and LLM-105 were found to have the highest fluorescence intensities and correlated with the amorphous/weakly graphitic carbon allotrope.

The presented Raman spectra of the soot is consistent with a model where the main variable for the spectral information is based on the amorphous carbon content in the samples.

Summary

Soot collected from the detonation of nine explosives was investigated with Raman spectroscopy and high-resolution transmission electron microscopy (HRTEM). The Raman spectra from the different types of detonation soot were found to differ significantly enough to provide unique signatures based on the type of explosive used. The variability in the spectra from analysis at multiple spots within each detonation soot was found to be small, aiding in differentiating among the explosives. Principal component analysis was used to map the differences between the different types of soot and in turn determine the type of explosive that created them. The spectral data suggest that the main change in the Raman spectra is based on the content of amorphous carbon affecting the baseline in the 1500 cm^{-1} region. Amorphous carbon content in the soot can be traced to the explosive used in the detonation. The thermodynamic conditions of the detonation were responsible for the different carbon allotropes and abundances in the soot. Results obtained with Raman spectroscopy were found to correlate with the HRTEM images. Images from TEM have shown that the different types of soot generated from the detonation of explosives can possess several forms of carbon. Laser-induced fluorescence from the samples also provided an additional signature to separate different types of soot. Soots from HNS IV and TNT without fluorescence occupy the same PCA space as the fluorescent HMX, Comp B, and DNTF. Initial data suggest that fluorescence can also help determine the origin of the soot.

Acknowledgements

This work was funded by the Office of Defense Nuclear Nonproliferation Research and Development within the U.S. Department of Energy's National Nuclear Security Administration under project FY21-ML-LL_PD2Cd-P106. Portions of this work were performed under the auspices of the U.S. Department of Energy by Lawrence Livermore National Laboratory under contract DE-AC52-07NA27344. TEM work utilized the Molecular Foundry, a DOE User Facility operated for the DOE Office of Science by Lawrence Berkeley National Laboratory under Contract No. DE-AC02-05CH11231. The authors thank Virginia Altoe and Shaul Aloni for the use of and assistance with the JEOL 2100F. This manuscript was authored by Savannah River National Laboratory and is operated by Battelle Savannah River Alliance for the U.S. Department of Energy under Contract No. 89303321CEM000080.The United States Government retains and the publisher, by accepting this article for publication, acknowledges that the United States Government retains a non-exclusive, paid-up, irrevocable, worldwide license to publish or reproduce the published form of this work, or allow others to do so, for United States Government purposes.

References

(1) Brunetto R, Pino T, Dartois E, Cao AT, d'Hendecourt L, Strazzulla G, Bréchignac P *Icarus* **2009**, *200*, 323.

(2) Dippel B, Jander H, Heintzenberg J *Physical Chemistry Chemical Physics* **1999**, *1*, 4707.

(3) Grafen M, Nalpantidis K, Platte F, Monz C, Ostendorf A *Aerosol Science and Technology* **2015**, *49*, 997.
(4) Herdman JD, Connelly BC, Smooke MD, Long MB, Miller JH *Carbon* **2011**, *49*, 5298.
(5) Sadezky A, Muckenhuber H, Grothe H, Niessner R, Pöschl U *Carbon* **2005**, *43*, 1731.
(6) Beyssac O, Goffé B, Petitet J-P, Froigneux E, Moreau M, Rouzaud J-N *Spectrochimica Acta Part A: Molecular and Biomolecular Spectroscopy* **2003**, *59*, 2267.
(7) Dippel B, Heintzenberg J *Journal of Aerosol Science* **1999**, *30*, S907.
(8) Lespade P, Marchand A, Couzi M, Cruege F *Carbon* **1984**, *22*, 375.
(9) Matthews MJ, Pimenta MA, Dresselhaus G, Dresselhaus MS, Endo M *Physical Review B* **1999**, *59*, R6585.
(10) Mernagh TP, Cooney RP, Johnson RA *Carbon* **1984**, *22*, 39.
(11) Robertson J *Advances in Physics* **1986**, *35*, 317.
(12) Tuinstra F, Koenig JL *The Journal of Chemical Physics* **1970**, *53*, 1126.
(13) Vidano RP, Fischbach DB, Willis LJ, Loehr TM *Solid State Communications* **1981**, *39*, 341.
(14) Wagner J, Ramsteiner M, Wild C, Koidl P *Phys Rev B Condens Matter* **1989**, *40*, 1817.
(15) Dasappa S, Camacho J *Fuel* **2021**, *291*, 120196.
(16) Commodo M, Joo PH, De Falco G, Minutolo P, D'Anna A, Gülder ÖL *Energy & Fuels* **2017**, *31*, 10158.
(17) Wang Y, Alsmeyer DC, McCreery RL *Chemistry of Materials* **1990**, *2*, 557.
(18) Sze SK, Siddique N, Sloan JJ, Escribano R *Atmospheric Environment* **2001**, *35*, 561.
(19) Cuesta A, Dhamelincourt P, Laureyns J, Martínez-Alonso A, Tascón JMD *Carbon* **1994**, *32*, 1523.
(20) Chan JW, Taylor DS, Zwerdling T, Lane SM, Ihara K, Huser T *Biophysical Journal* **2006**, *90*, 648.
(21) Feng S, Chen R, Lin J, Pan J, Chen G, Li Y, Cheng M, Huang Z, Chen J, Zeng H *Biosensors and Bioelectronics* **2010**, *25*, 2414.
(22) Yang H, Irudayaraj J, Paradkar MM *Food Chemistry* **2005**, *93*, 25.
(23) Bro R, Smilde AK *Analytical Methods* **2014**, *6*, 2812.
(24) Lever J, Krzywinski M, Altman N *Nature Methods* **2017**, *14*, 641.
(25) Hammons JA, Nielsen MH, Bagge-Hansen M, Bastea S, Shaw WL, Lee JRI, Ilavsky J, Sinclair N, Fezzaa K, Lauderbach LM, Hodgin RL, Orlikowski DA, Fried LE, Willey TM *The Journal of Physical Chemistry C* **2019**, *123*, 19153.
(26) Faccinetto A, Irimiea C, Minutolo P, Commodo M, D'Anna A, Nuns N, Carpentier Y, Pirim C, Desgroux P, Focsa C, Mercier X *Communications Chemistry* **2020**, *3*, 112.
(27) daFonseca BG, Thind SS, Brolo AG *Journal of Raman Spectroscopy* **2021**, *52*, 516.
(28) Casiraghi C, Piazza F, Ferrari AC, Grambole D, Robertson J *Diamond and Related Materials* **2005**, *14*, 1098.
(29) Knight DS, White WB *Journal of Materials Research* **2011**, *4*, 385.
(30) Nakamura K, Fujitsuka M, Kitajima M *Physical Review B* **1990**, *41*, 12260.
(31) Mapelli C, Castiglioni C, Meroni E, Zerbi G *Journal of Molecular Structure* **1999**, *480-481*, 615.
(32) Dresselhaus MS, Dresselhaus G *Advances in Physics* **1981**, *30*, 139.
(33) Al-Jishi R, Dresselhaus G *Physical Review B* **1982**, *26*, 4514.
(34) Jawhari T, Roid A, Casado J *Carbon* **1995**, *33*, 1561.
(35) Gruber T, Zerda TW, Gerspacher M *Carbon* **1994**, *32*, 1377.
(36) Popov M, Churkin V, Kirichenko A, Denisov V, Ovsyannikov D, Kulnitskiy B, Perezhogin I, Aksenenkov V, Blank V *Nanoscale Research Letters* **2017**, *12*, 561.

(37) Kashkarov AO, Pruuel ER, Ten KA, Rubtsov IA, Gerasimov EY, Zubkov PI *Journal of Physics: Conference Series* **2016**, *774*, 012072.
(38) Hammons JA, Nielsen MH, Bagge-Hansen M, Lauderbach LM, Hodgin RL, Bastea S, Fried LE, Cowan MR, Orlikowski DA, Willey TM *Propellants, Explosives, Pyrotechnics* **2020**, *45*, 347.
(39) Hammons JA, Nielsen MH, Bagge-Hansen M, Bastea S, May C, Shaw WL, Martin A, Li Y, Sinclair N, Lauderbach LM, Hodgin RL, Orlikowski DA, Fried LE, Willey TM *The Journal of Physical Chemistry Letters* **2021**, *12*, 5286.
(40) Bagge-Hansen M, Bastea S, Hammons JA, Nielsen MH, Lauderbach LM, Hodgin RL, Pagoria P, May C, Aloni S, Jones A, Shaw WL, Bukovsky EV, Sinclair N, Gustavsen RL, Watkins EB, Jensen BJ, Dattelbaum DM, Firestone MA, Huber RC, Ringstrand BS, Lee JRI, van Buuren T, Fried LE, Willey TM *Nature Communications* **2019**, *10*, 3819.
(41) Qian X, Wang X, Zhong J, Zhi J, Heng F, Zhang Y, Song S *Journal of Raman Spectroscopy* **2019**, *50*, 665.
(42) Mermoux M, Chang S, Girard HA, Arnault J-C *Diamond and Related Materials* **2018**, *87*, 248.
(43) Chaudhuri SN, Chaudhuri RA, Benner RE, Penugonda MS *Composite Structures* **2006**, *76*, 375.
(44) Filik J, May PW, Pearce SRJ, Wild RK, Hallam KR *Diamond and Related Materials* **2003**, *12*, 974.
(45) Ferrari AC, Robertson J *Physical Review B* **2000**, *61*, 14095.
(46) Codorniu Pujals D, Arias de Fuentes O, Desdín García LF, Cazzanelli E, Caputi LS *Applied Physics A* **2015**, *120*, 1339.
(47) Roy D, Chhowalla M, Wang H, Sano N, Alexandrou I, Clyne TW, Amaratunga GAJ *Chemical Physics Letters* **2003**, *373*, 52.
(48) Nandi AK, Kasar SM, Thanigaivelan U, Ghosh M, Mandal AK, Bhattacharyya SC *Journal of Energetic Materials* **2007**, *25*, 213.
(49) Ramsteiner M, Wagner J *Applied Physics Letters* **1987**, *51*, 1355.
(50) Nemanich RJ, Solin SA *Physical Review B* **1979**, *20*, 392.
(51) van der Heijden AEDM, Bouma RHB *Crystal Growth & Design* **2004**, *4*, 999.
(52) Feng-qi Z, Pei C, Rong-zu H, Yang L, Zhi-zhong Z, Yan-shui Z, Xu-wu Y, Yin G, Sheng-li G, Qi-zhen S *Journal of Hazardous Materials* **2004**, *113*, 67.
(53) Pérez-Ojeda ME, Castro E, Kröckel C, Lucherelli MA, Ludacka U, Kotakoski J, Werbach K, Peterlik H, Melle-Franco M, Chacón-Torres JC, Hauke F, Echegoyen L, Hirsch A, Abellán G *Journal of the American Chemical Society* **2021**, *143*, 18997.
(54) Viswanath DS, Ghosh TK, Boddu VM In *Emerging Energetic Materials: Synthesis, Physicochemical, and Detonation Properties*; Viswanath DS, Ghosh TK, Boddu VM, Eds.; Springer Netherlands: Dordrecht, 2018, p 213.
(55) Hamilton BW, Steele BA, Sakano MN, Kroonblawd MP, Kuo IFW, Strachan A *The Journal of Physical Chemistry A* **2021**, *125*, 1766.
(56) Anniyappan M, Talawar MB, Gore GM, Venugopalan S, Gandhe BR *Journal of Hazardous Materials* **2006**, *137*, 812.
(57) Dimitris Kyprianou MB, Giovanni Emma, Grzegorz rarata, David Anderson, Gabriela Diaconu, Vassiliki Exarchou *Molecules* **2020**, *25*, 3586.

Table 1. Summary of the explosives used, the chemical formula, and the type of carbon found in each soot.

Explosive	Chemical Formula	Carbon Form

UFTATB[48]	$C_6H_6N_6O_6$	Amorphous[11,14,44,45,49]/weakly graphitic[12,30,31,50]
TATB[48]	$C_6H_6N_6O_6$	Amorphous[11,14,44,45,49]/weakly graphitic[12,30,31,50]
HMX[51]	$C_4H_8N_8O_8$	Amorphous[11,14,44,45,49]/weakly graphitic/graphite sheets[12,30,31,50]/graphite fibers[41,43]/diamond[36,42]
DNTF[52]	$C_6N_8O_8$	Carbon onions[46,47,53]
HNS IV[54]	$C_{14}H_6N_6O_{12}$	Graphite fibers[41,43]
Comp B[51]	60% $C_3H_6N_6O_6$ 40% $C_7H_5N_3O_6$	nanodiamonds[36,42]
LLM-105[55]	$C_4H_4N_6O_5$	Amorphous[11,14,44,45,49]/weakly graphitic/graphite[12,30,31,50]/diamond[36,42]
FOX-7[56]	$C_2H_4N_4O_4$	Graphite[12,30,31,50]
TNT[57]	$C_7H_5N_3O_6$	Graphite [12,30,31,50]

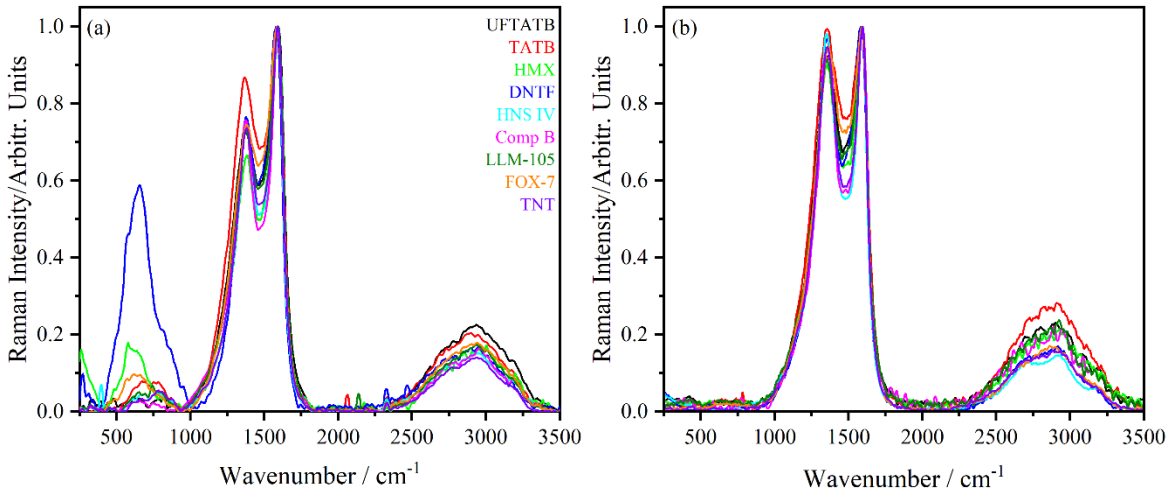

Figure 1. a) Representative spectra baseline corrected for each soot collected with a 405 nm excitation laser. b) Representative spectra baseline corrected for each soot collected with a 514 nm excitation laser

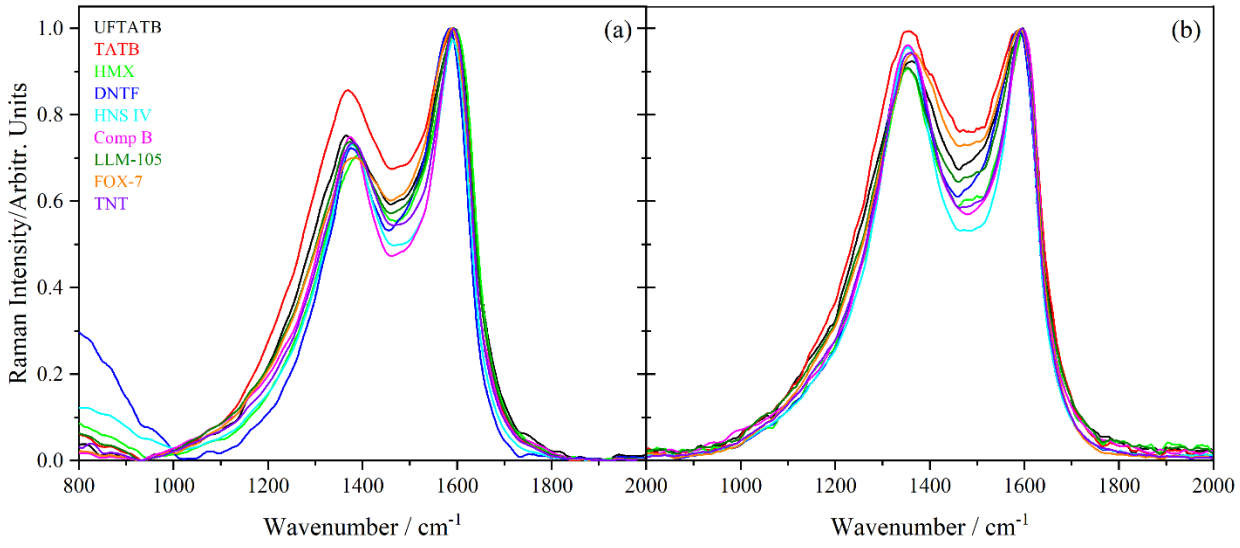

Figure 2. Baseline corrected and averaged Raman spectra of soot from different types of explosives acquired with the a) 405 nm and b) 514 nm excitation lasers.

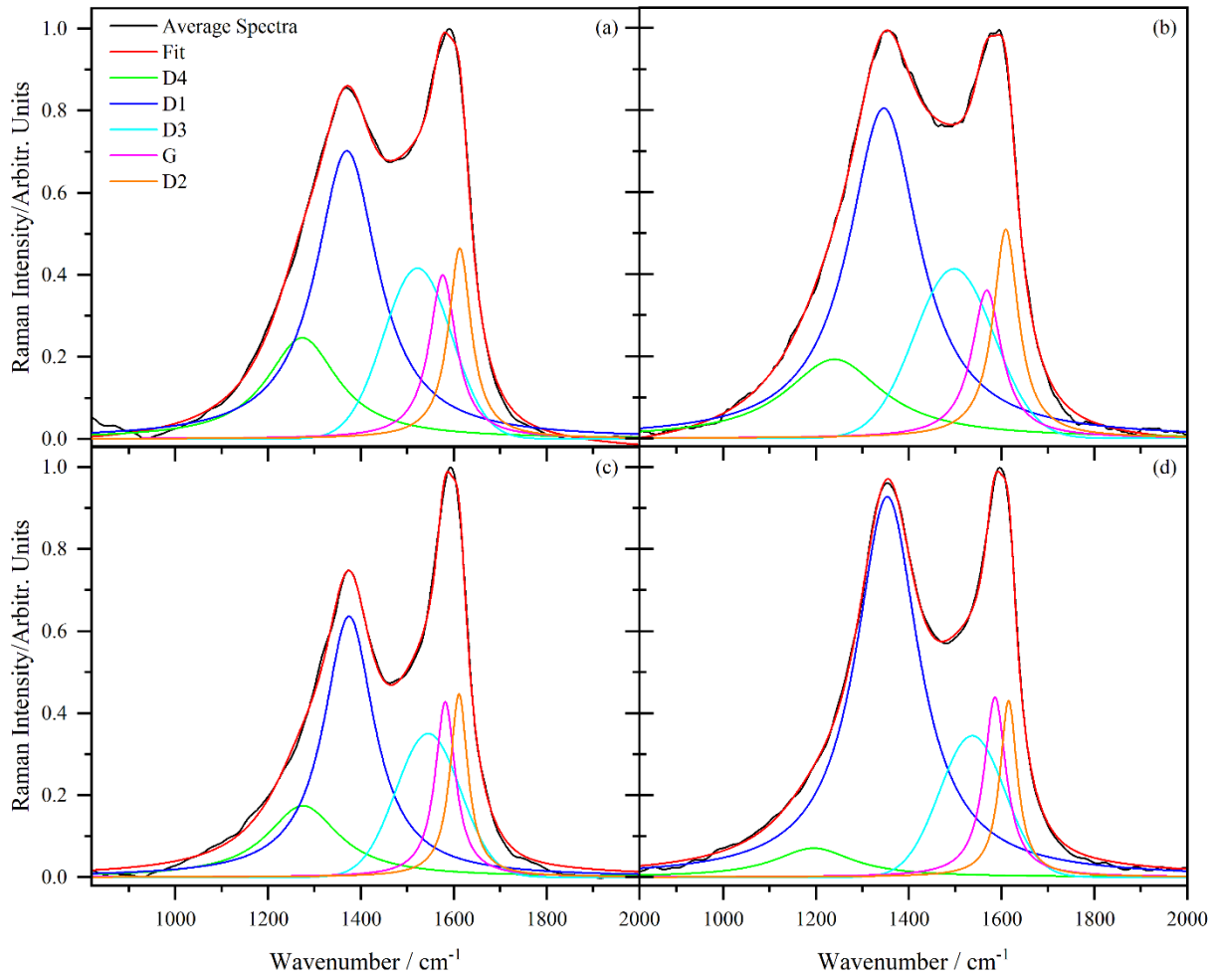

Figure 3. Curve fitting for detonation soots of a) TATB with λ = 405 nm b) TATB with λ = 514 nm c) Comp B with λ = 405 nm, and d) Comp B with λ = 514 nm. TATB was found to have the largest amorphous carbon content and Comp B was found to have lowest.

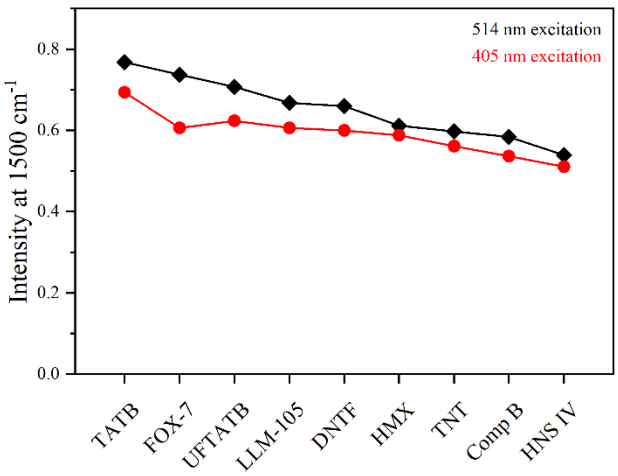

Figure 4. Spectral intensity of valley region (1500 cm^{-1}) from averaged soot spectra for the 405 and 514 nm excitation laser wavelengths.

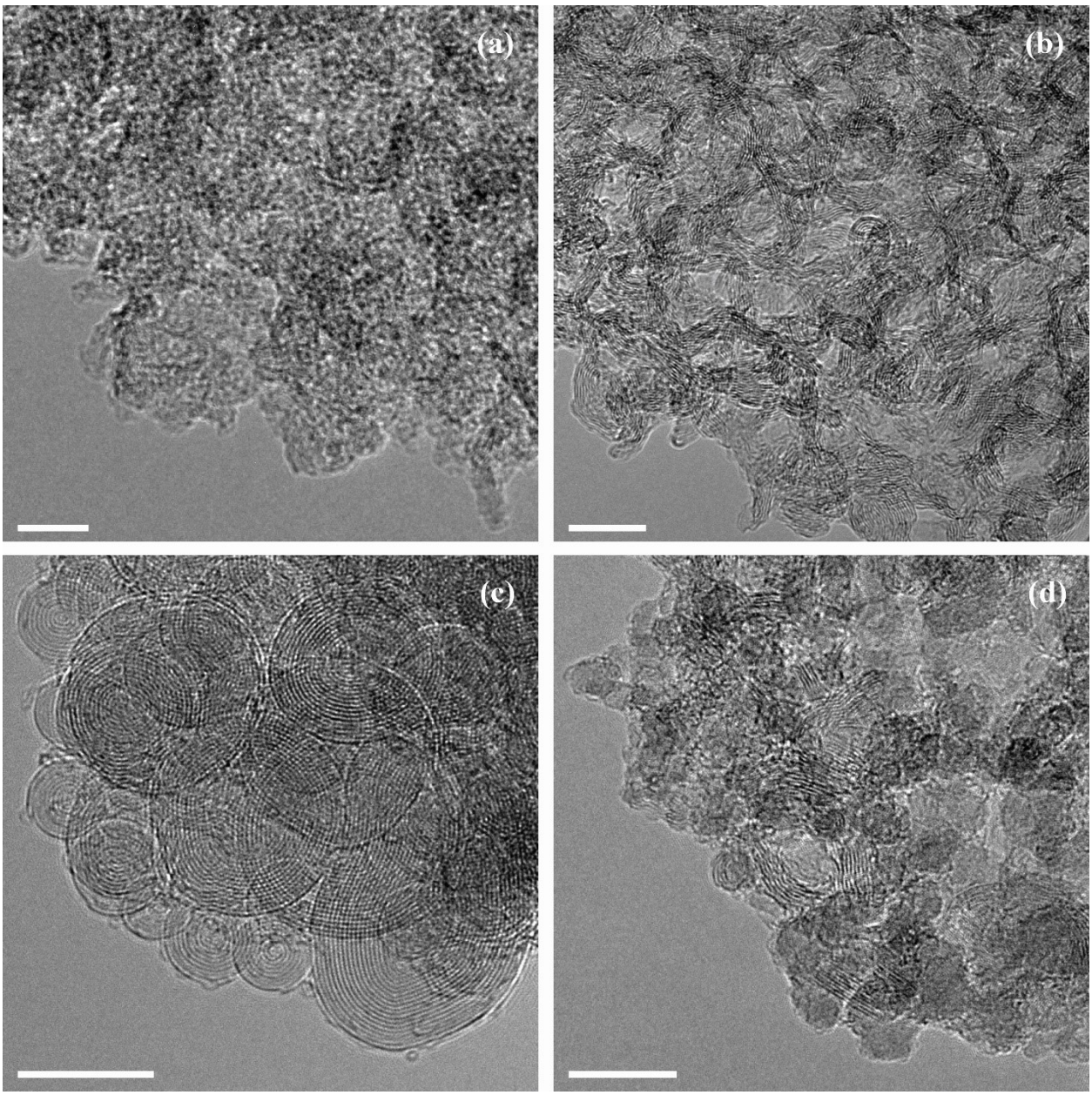

Figure 5. Representative HRTEM images of typical structures observed for different categories of carbon nanostructures observed in the soots. Amorphous carbon from UFTATB (a), graphite fibers from HNS IV (b), onion-like carbon from DNTF (c), and nanodiamond with some graphite fibers from Comp B (d). Scale bars are 10 nm.

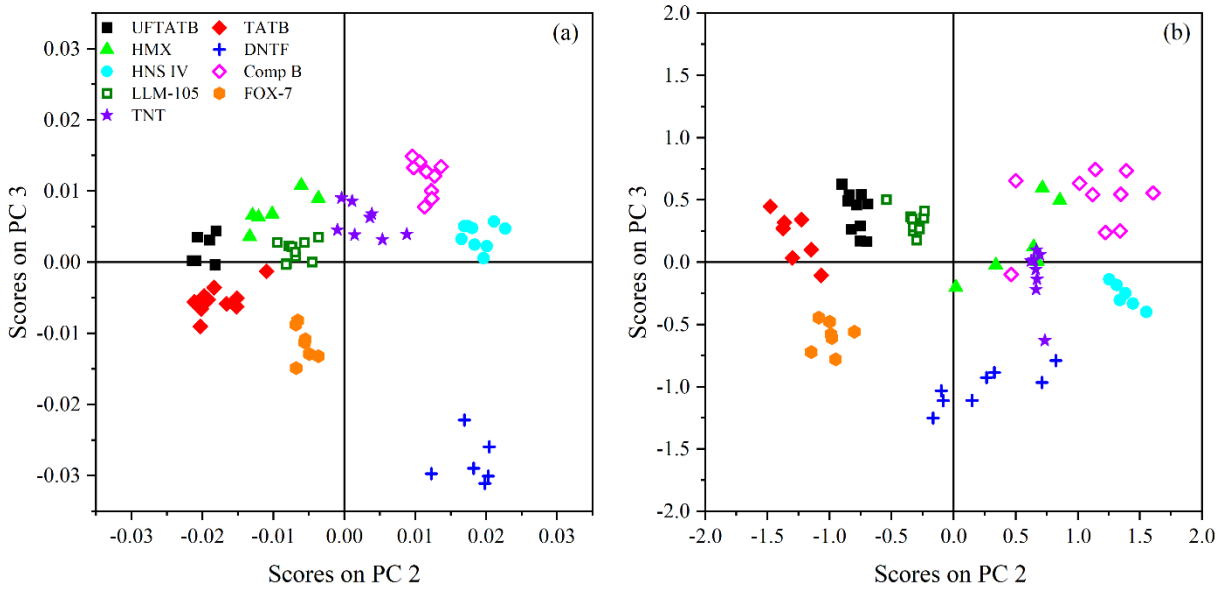

Figure 6. The scores plot of PC3 vs. PC2 are shown for a) data acquired with the 405 nm excitation laser and b) data acquired with the 514 nm excitation laser.